Environmental Modelling and Software 145 (2021) 105182

Contents lists available at ScienceDirect

Environmental Modelling and Software

journal homepage: www.elsevier.com/locate/envsoft

Evaluation of surface wind using WRF in complex terrain: Atmospheric input data and grid spacing

Kine Solbakken [a,*], Yngve Birkelund [a], Eirik Mikal Samuelsen [a,b]

[a] UiT, The Arctic University of Norway, Norway
[b] Norwegian Meteorological Institute, Tromsø, Norway

ARTICLE INFO

Keywords:
Wind resource assessment
WRF model
ERA5
ERA-Interim
Complex terrain
Grid resolution

ABSTRACT

This study evaluates a numerical weather prediction model as a tool for wind resource assessment in complex terrain and how the simulations are affected by the selection of initial and boundary conditions and various grid resolutions. Two global reanalyses, ERA-Interim and ERA5, and four grid resolutions, 27 km, 9 km, 3 km and 1 km, have been considered. The simulations have been compared to hub-height wind measurements. The ERA5 forced simulations were found to provide improved wind speed results. The simulations show clear improvements in terms of lower error when the grid spacing is reduced from 27 km via 9 km to 3 km. From 3 km to 1 km, the error is not further reduced. However, the 1 km simulations tend to better reproduce the mean wind features and show defined areas with higher and lower wind speeds, providing useful information for wind resource mapping in complex terrain.

1. Introduction

A mesoscale numerical weather prediction (NWP) model is a mathematical representation of the physical and dynamical processes in the atmosphere on scales ranging from a few kilometres and up to a couple of thousands kilometres (Jacobson, 2005). The models were originally developed for weather forecasting applications, but have also emerged as a useful tool for the wind power sector as it can provide the users with high resolution wind climatology over large areas (Jacobson, 2005; Carvalho et al., 2012b; Mughal et al., 2017; Carvalho et al., 2014). Wind data retrieved from the mesoscale NWP model simulations can assist wind power agents in identifying areas with favourable wind conditions and accompany local wind measurement campaigns to determine long term climatology (Carvalho et al., 2012b; Mughal et al., 2017).

The NWP models represent an approximation of the real state of the atmosphere. The size of the deviation between the real and the simulated atmosphere depends e.g. on the model configurations, such as the choice of parametrization schemes for unresolved physical processes, terrain and vegetation representation, definition of the model domain size, location and spatial resolution, numerical options and initial and boundary conditions (Awan et al., 2011). Through a careful model configuration, the user is able to optimise the model for one specific area or weather event. For wind energy purposes, it is especially important to limit and identify how the model deviates from the real atmosphere, as a small error in the wind speed will induce a large error in the wind energy estimate. In particular, in our study, special attention will be given to the dependency on the input atmospheric data and the model resolution. Both are expected to have a crucial impact on the ability of the model to reproduce the wind in the selected study area, characterised by a coastal and mountainous terrain, located within the Arctic region.

For mesoscale NWP models, the input atmospheric data give initialisation fields and boundary conditions throughout the simulation time, and are typically provided by global reanalysis data (Carvalho et al., 2014). The global reanalyses are obtained through global NWP models that optimally combine meteorological observations with model forecasts through an assimilation process into a physical coherent description of the evolution of the atmosphere (Dee et al., 2011; Hersbach et al., 2020). The Arctic region is particularly challenging for global reanalyses due to few observations from weather stations available for assimilation and evaluation (Wesslén et al., 2014; Inoue et al., 2015). In addition, the parametrization in the forecasting model is not tuned for phenomena unique to the Arctic (Wesslén et al., 2014). A careful evaluation of the global reanalysis used to force the simulations are therefore considered to be especially important for the area of interest in this paper. Two global reanalysis products will be considered, the ERA-Interim (ERA-I) and the ERA5, both produced by the European

* Corresponding author.
E-mail address: kine.solbakken@uit.no (K. Solbakken).

https://doi.org/10.1016/j.envsoft.2021.105182
Accepted 24 August 2021
Available online 4 September 2021

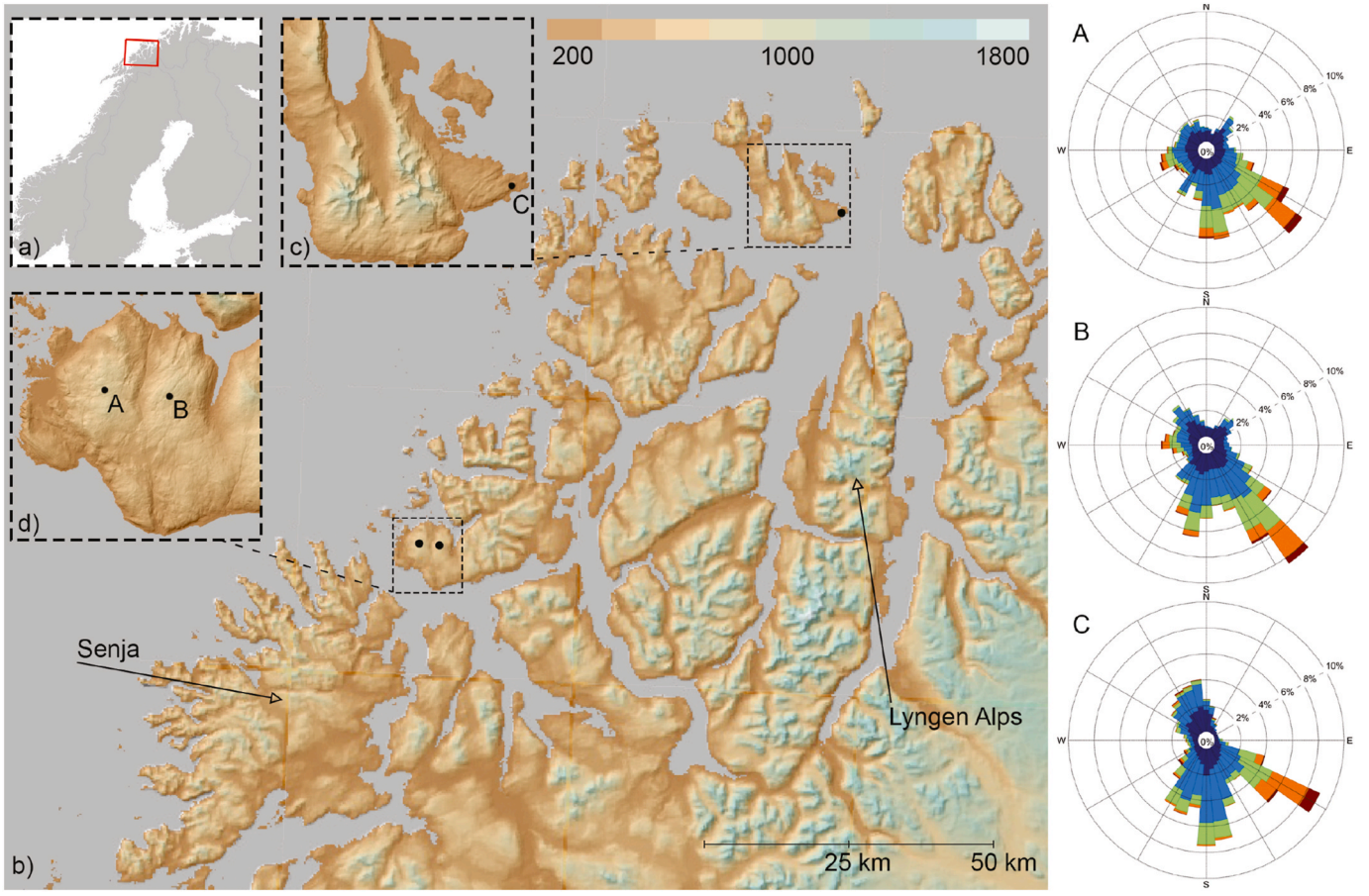

Fig. 1. a) Red square outlines the study area and (Fig. 1b). Land area (Norway, Sweden and Finland) in grey and ocean in white. b) Relief map of the topography in the study area. The altitude is indicated by colours from brown to light blue as given in the colour bar. Surrounding ocean in flat grey. Black dotted squares outline (Fig. 1c) and (Fig. 1d). c) Zoomed view of location C. The dot indicates the position of the met mast. d) Zoomed relief view of location A (left dot) and B (right dot). The wind roses present the measured wind data from location A (top), B (middle) and C (bottom).

Centre for Medium-Range Weather Forecasts (ECMWF). Several energy related studies have evaluated and compared ERA-I and other global reanalyses as input data for mesoscale simulations, and found that ERA-I forced simulations tend to provide a better representation of the wind field (Mughal et al., 2017; Carvalho et al., 2014; Fernández-González et al., 2018; Menéndez et al., 2011; Carvalho et al., 2012a). The most recent global reanalysis by the ECMWF, ERA5, benefits from 10 years of development in the forecasting model and the data assimilation method (Hersbach et al., 2020). In addition, ERA5 also typically assimilate a higher number of observations than ERA-I. The great strength of ERA5 in comparison with ERA-I, is expected to be due to the increased spatial and temporal resolution (Hersbach et al., 2020). A horizontal resolution of 31 km, 137 vertical layers and an hourly data output, realize a more detailed description of the atmosphere and its evolution (Hersbach et al., 2020), in comparison to the 80 km horizontal resolution, 60 vertical layers and the 6-h output resolution of ERA-I (Dee et al., 2011). Several studies report that ERA5 outperforms ERA-I and several other global reanalyses in the representation of surface wind, both over land (Olauson, 2018; Ramon et al., 2019) and over oceans (Belmonte Rivas and Stoffelen, 2019). Particularly encouraging in relation to our study, are the results provided by (Graham et al., 2019) where wind data from five atmospheric reanalyses, including ERA-I and ERA5, were evaluated with respect to wind speed measurements in the Arctic. It was found that ERA5 provided the best results for wind speed, with the highest correlation and smallest bias and Root-Mean-Square Error (RMSE).

The second essential factor for mesoscale wind simulations that will be considered in this study is the model resolution. The study area is characterised by steep mountains, fjords and numerous islands. Within the field of numerical weather prediction, this terrain is typically described as complex, and numerical simulations over such areas remain challenging (Carvalho et al., 2012b; Mughal et al., 2017; Carvalho et al., 2014; Krieger et al., 2009). The air flow in coastal zones is typically strongly affected by the abrupt change in temperature and frictional drag between land and sea areas (National Research Council, 1992). Depending on several factors such as the stability of the atmosphere and the wind speed, the coastal orography may give rise to complex flow patterns such as blocking, strong gap winds and mountain waves with downslope wind storms (National Research Council, 1992). The model representation of the terrain is considered to be an important key factor for achieving a good representation of the wind flow in complex terrain (Carvalho et al., 2012b; Mughal et al., 2017). Previous studies indicate that higher resolution tends to give better wind simulations results in complex terrain (Carvalho et al., 2012b; Mughal et al., 2017; Fernández-González et al., 2018; Carvalho et al., 2012a; Samuelsen, 2007; Valkonen et al., 2020). The drawback of higher resolution is the computational cost and also the possibility of phase errors (Mass et al., 2002).

This study will assess the possible improvement in the wind speed simulations when WRF is forced by ERA5, compared to when it is forced by ERA-I. A second focus will be on how different model resolutions affect the ability to reproduce the wind field over the area of interest. The wind simulations will be compared to hub-height measurements at three different locations. The rest of the paper is structured as follows: Section 2 describes the method of the study, including a description of the measurements, the configuration of the WRF model as well as the statistical metric used for evaluation. The results and the discussion are

Table 1
The geographical location of the three meteorological masts, RIX values at the mast locations and the true elevation (Z) compared to the model elevation in the four domains. The elevation is given in masl.

Location	Lat.	Lon.	RIX	Z	D01	D02	D03	D04
A	69.59	18.12	10–20	550	118	134	237	468
B	69.58	18.21	10–20	505	132	180	321	430
C	70.09	20.09	5–10	68	79	66	18	32

presented in Section 3, while Section 4 provides a concluding summary.

2. Method

2.1. Study area and field measurements

The area considered in this study is located along the coast in the northern part of Norway as illustrated by the red square in (Fig. 1a). Large seasonal variations in the temperature over northern Scandinavia give rise to a monsoon-like wind pattern on the coast of Norway (Svendsen, 1995). During the winter season, cold air over land and warm air over the ocean, due to the North Atlantic Current, sets up a pressure gradient in east-west direction, with high pressure over land and low pressure over the ocean. During the summer season, the temperature and pressure gradients are often reversed. This results in a main wind direction from the southeast (SE) during the winter, and from northeast (NE) during the summer (Svendsen, 1995). In addition to the pressure gradient due to the difference between temperature over land and over ocean, the polar front is a source of eastward-moving low-pressure systems. Especially during the winter season, when the horizontal temperature gradient across the polar front is largest, leading to baroclinic instability and frequently occurring strong low-pressure systems, there will be large variations in wind speed and directions in this area. The wind patterns will also be affected by the local topography and lead to topographically induced variations in the main wind directions. To illustrate that the seasonal variations in pressure and wind patterns also occur during the selected study period, from 1 September 2014 to 30 August 2015, the mean sea level pressure (MSLP) for the winter months (September 2014–March 2015) and the summer months (April 2015–August 2015) are presented in Figure A1 in the Appendix.

The relief map in (Fig. 1b) shows an overview of the terrain in the study area, with mountainous islands and peninsulas separated by long fjords and sounds. The mountains in the area range from sea level and up to about 1800 m above sea level (masl.). The wind measurements used to analyse the model performance were collected from three different coastal locations, referred to as location A, B and C, with mean measured wind speeds during the study period of 7.38 ms^{-1}, 7.10 ms^{-1} and 7.72 ms^{-1}, respectively. The coordinates, the terrain ruggedness index (RIX) (Bowen et al., 1996) and the elevation above sea level of the locations are summarized in Table 1. The RIX describes the fraction of the area within a 2 km radius with slopes steeper than 30% (Berge et al., 2006). The RIX presented in this study have been collected from a wind resource report provided by The Norwegian Water Resources and Energy Directorate (NVE) (Byrkjedal and Åkervik, 2009).

Fig. 1d, shows a close up map with two dots where the left dot indicates location A and the right dot location B. The two masts, in location A and B, are situated only 3.5 km apart, on two rather flat mountain peaks, at 550 masl. and 505 masl. respectively. The two mountains are separated by a narrow valley with elevations below 200 masl. The masts at A and B have similar configurations, with measurements 80 m above ground level (magl.). The data sets from location A(B) spanning a full year of measurements consists of 95.4% (98.9%) data relative to a full time series in the same period with the same sampling frequency. At both A and B, all measurements are recorded during the wind resource assessment phase, before any construction of the wind farm, and are therefore free of any wake disturbances from wind turbines.

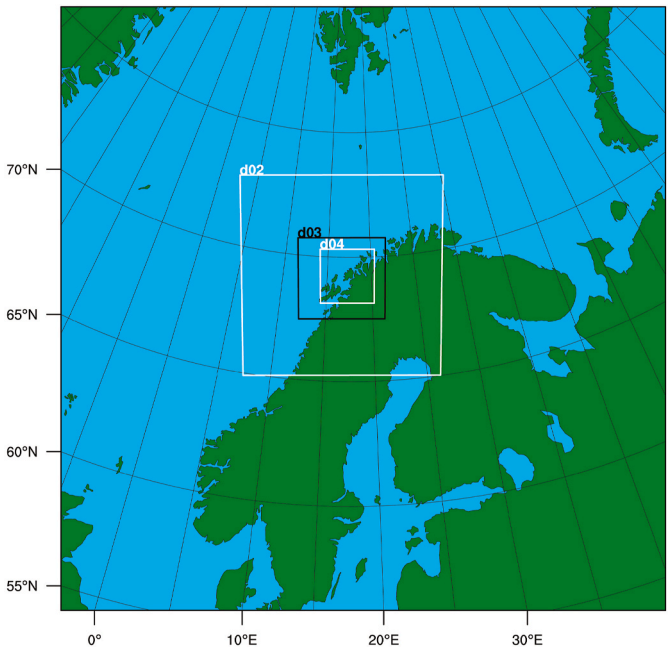

Fig. 2. The WRF domain configuration, D01, D02, D03 and D04.

Mast C, depicted by a black dot in (Fig. 1c), is situated at 68 masl. on a rather small island. The large mountains 5 km west of the mast, reach up to 1000 masl. and may partially work as an orographic blockage of westerly winds. The Lyngen Alps, a 90 km long mountain range separating two long fjords, just south of location C, is also expected to have a large impact on the wind at this location. The wind measurements are done at 80 magl. and has a data availability higher than 99.9%. The mast is situated nearby an operational wind farm consisting of 18 wind turbines with hub height of 80 m and rotor diameter of 90 m. The main wind direction is from the SE and all the turbines are located north and west of the mast.

The measured data used in this study, have a temporal resolution of 10 min. The study period from 1 September 2014 to 30 August 2015 was selected because this period had the best coverage of measurements for all three locations.

2.2. Numerical weather model

In this study the Advanced Weather Research and Forecasting (WRF) model version 3.9.1 is used. This is a three dimensional, nonhydrostatic mesoscale model developed by the National Centre for Atmospheric Research (NCAR). The model is widely used for research on atmospheric processes as well as for numerical weather prediction (NWP). A detailed description of the model may be found in Skamarock et al. (2008).

For the purpose of this study, the model is configured to include four one-way nested domains, D01, D02, D03 and D04, with a horizontal resolution of 27 km, 9 km, 3 km, and 1 km, respectively (Fig. 2). Polar stereographic projection has been applied, as recommended for high latitude areas, and the outer domain is centred at 67°56′N and 17°39′E. The vertical structure of all domains consist of 50 terrain-following sigma levels with an upper boundary at 50 hPa. In order to describe the terrestrial fields, information about the topography, land-water mask and land use have been interpolated to the model grid from the 20-category Moderate Resolution Imaging Spectroradiometer (MODIS) land use data and the Global Multi-resolution Terrain Elevation Data 2010 (GMTED 2010). Both data sets were retrieved from the NCAR database and have a 30 arc-second resolution. To represent the physical processes that are not explicitly resolved by the model, the NCAR Convection-Permitting suite (CONUS) has been applied for all domains.

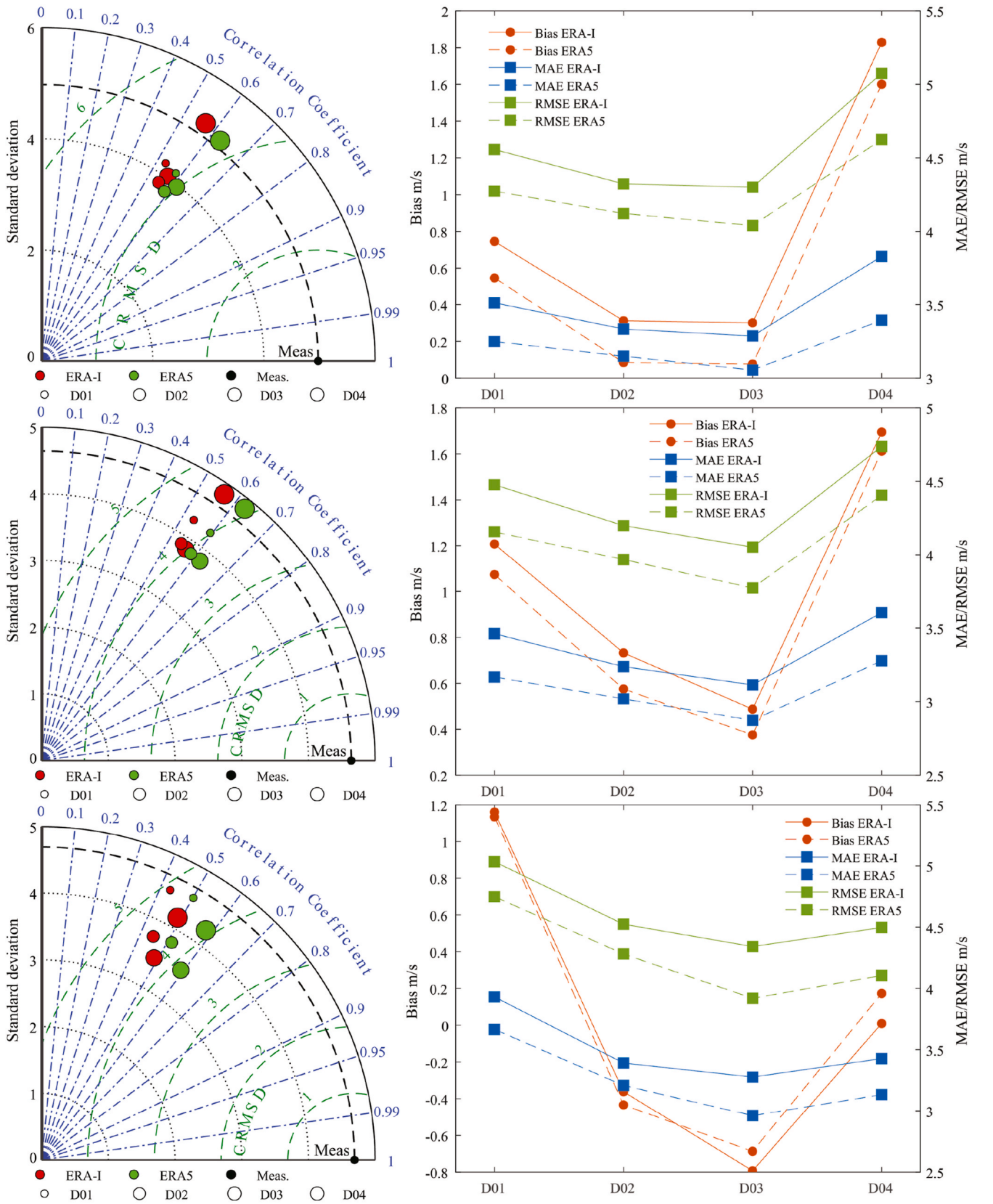

Fig. 3. Left column: Taylor diagrams presenting SD, CRMSE and R. The size of the dot indicates the domain, see legend on the bottom of the figure. Right column: Graphs presenting MAE, RMSE (right axis), and Bias (left axis). The evaluation metrics for location A in the top row, B in the middle and C at the bottom row.

The CONUS suite consist of the Thompson microphysics scheme (Thompson et al., 2008), the Mellor-Yamada-Janjic (MYJ) planetary boundary layer (PBL) scheme (Janjić, 1994), the Noah land surface model (Chen et al., 1997), the rapid radiative transfer model for global applications (RRTMG) shortwave and longwave radiations schemes (Iacono et al., 2008), the Tiedtke cumulus scheme (Tiedtke, 1989; Zhang et al., 2011) and the MYJ surface layer scheme (Janjić, 1994). This combination of parametrization schemes has been developed and tested over several years until released as a physics suite in 2016 (Powers et al., 2017; Romine et al., 2013).

The time period considered in this study covers a full year. For simulations over long time periods, it is recommended to run several shorter simulations, to avoid accumulation of truncation errors (Carvalho et al., 2012b). To achieve a full year of model data, the WRF simulations were initialised 52 times and run for 8 days at the time, hereinafter referred to as a week. The first 12 h of the simulations were considered spin up time and therefore discharged. The following 12 h were combined with the last 12 h from the previous week by linear interpolation to assure a smooth curve.

The model has been run with a time step of 81 s for D01, and reduced by a factor of 3 for each of the following nests. Outputs were saved every 10th minute. The model was run twice, first with ERA-I, and second with ERA5, as initial and boundary conditions. The boundary conditions are updated throughout the simulation time. For the simulations initialised with ERA-I, and for 35 of the 52 weeks initialised by ERA5, the model ran without problems. However, for the remaining 17 weeks initialised by ERA5 the model became unstable. This problem was solved by either introducing damping, such as time off-centring, vertical velocity damping, and divergence damping, or by running the model with adaptive time step.

The wind data considered in this study are retrieved in the vertical by interpolation of the model-level wind to 80 magl. and in the horizontal by bilinear interpolation of the grid points to the exact geographical location of the observation points.

2.3. Evaluation metrics

In order to evaluate the performance of the different model configurations, the following statistical metrics are used; bias, Standard Deviation (SD), Mean Absolute Error (MAE), Root-Mean Square Error (RMSE), Centred Root-Mean Square Error (CRMSE) and correlation coefficient (R). The bias, the MAE and the RMSE are calculated as given in (Wilks, 2011), while the CRMSE, the R and the SD as given in (Taylor, 2001) and are all repeated in this section.

Let x_i be a time series consisting of $i = 1, 2, \ldots, N$ data points. The mean ($\bar{x}$) and the SD of these time series is estimated as:

$$\bar{x} = \frac{1}{N}\sum_{i=1}^{N} x_i \tag{1}$$

$$SD = \sqrt{\frac{\sum_{i=1}^{N}(x_i - \bar{x})^2}{N}} \tag{2}$$

The SD is a measure of the dispersion of the values in a data set. Simulations with values close to the ones in the measurements are desired.

The bias describes the tendency of the model to systematically over- or underestimate a parameter. Thus, a negative value indicates that the model tends to underestimate the parameter, i.e. the wind speed in this study, and a positive value the opposite. The bias between two time series, x_i and y_i is defined as

$$d = \frac{1}{N}\sum_{i=1}^{N} x_i - y_i \tag{3}$$

where y_i normally is taken as the true value. Here, x and y represent the simulation and measurement data, respectively.

The correlation coefficient indicates if there is a linear relationship between two time series and are given by the following relationship:

$$R = \frac{\frac{1}{N}\sum_{i=1}^{N}(x_i - \bar{x})(y_i - \bar{y})}{SD_x SD_y} \tag{4}$$

If R equals 1, the highest possible value, the pattern of the two time series is exactly the same. However, the amplitude might still be different, i.e. the bias might be non-zero. If R equals 0, there is no linear correlation between the two data sets.

The MAE, the RMSE and the CRMSE all describes the magnitude of the error between a measured and a simulated parameter. If the pattern, the phase and the amplitude of two time series are exactly identical, the MAE, the RMSE and the CRMSE equals zero. The MAE describes the total error between the measurements and the simulation without considering the sign of the error. The RMSE, is similar to the MAE, however, more sensitive to larger errors. The CRMSE is different from the MAE and the RMSE, in the way that the CRMSE is calculated without the tendency of the model to over- or underestimate. The MAE, the RMSE and the CRMSE are calculated from the following equations:

$$MAE = \frac{1}{N}\sum_{i=1}^{N}|x_i - y_i| \tag{5}$$

$$RMSD = \left\{\frac{1}{N}\sum_{i=1}^{N}(x_i - y_i)^2\right\}^{1/2} \tag{6}$$

$$CRMSD = \left\{\frac{1}{N}\sum_{i=1}^{N}[(x_i - \bar{x}) - (y_i - \bar{y})]^2\right\}^{1/2} \tag{7}$$

3. Results and discussion

3.1. Evaluation of the initial and boundary conditions

The CRMSE, the SD and the R between the measured data and the WRF simulations with different initialisation data, have been summarized in Taylor diagrams (Taylor, 2001) in the left column in Fig. 3 for location A, B and C, from all the domains. The statistical evaluation metrics are represented with coloured dots of different sizes. WRF initialised with ERA-I is depicted by red dots and WRF forced by ERA5 with green dots. The smallest dot represents domain D01, while the increasing sizes represent D02 and D03, and eventually D04 by the largest dot. The black dot represents the SD of the measurements. In the right column of Fig. 3, the bias, the RMSE and the MAE, are presented for each location. The solid lines represent the simulations forced by ERA-I and the dotted lines the simulations forced by ERA5. For more details, all the statistical evaluation metrics are also presented in the Appendix Table A1 at the end of this paper.

From the Taylor diagrams in Fig. 3 it is evident that WRF initialised with ERA5 reproduces the temporal pattern of the measured wind speed better than WRF forced with the ERA-I, in terms of lower CRMSE and higher R for all locations and all domains. Also, the RMSE and the MAE, presented as graphs in the right column in Fig. 3, indicate that the ERA5 forced simulations reproduces the wind speed better than the ERA-I driven simulations.

The wind speed bias of the model in this study are presented in the right column in Fig. 3. For location A and B the models tend to overestimate the wind speed, but the bias is found to be lower for the ERA5 forced simulations (red dotted line) compared to the ones forced by ERA-I (red solid line). In location C, there are only small differences between the models forced by ERA5 relative to those forced by ERA-I. The SD of the simulations, in comparison with the SD of the measurements, (left column Fig. 3), indicate how well the models are able to reproduce the wind speed variations. In this study, at these three

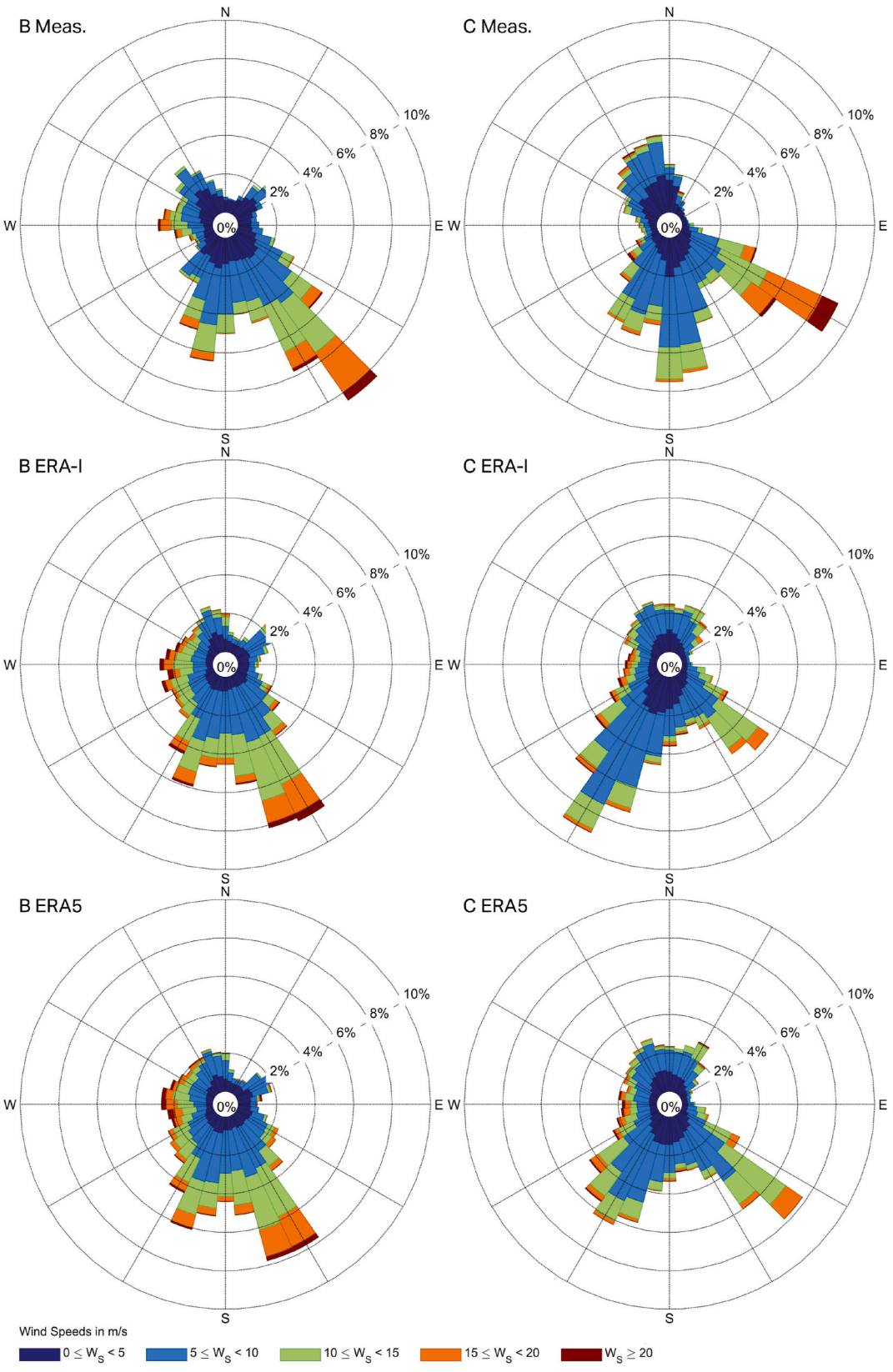

Fig. 4. Wind roses for D04, location B (left) and C (right). First row: Wind Measurements (Meas.). Second row: Simulations forced by ERA-I. Last row: Simulations forced by ERA5.

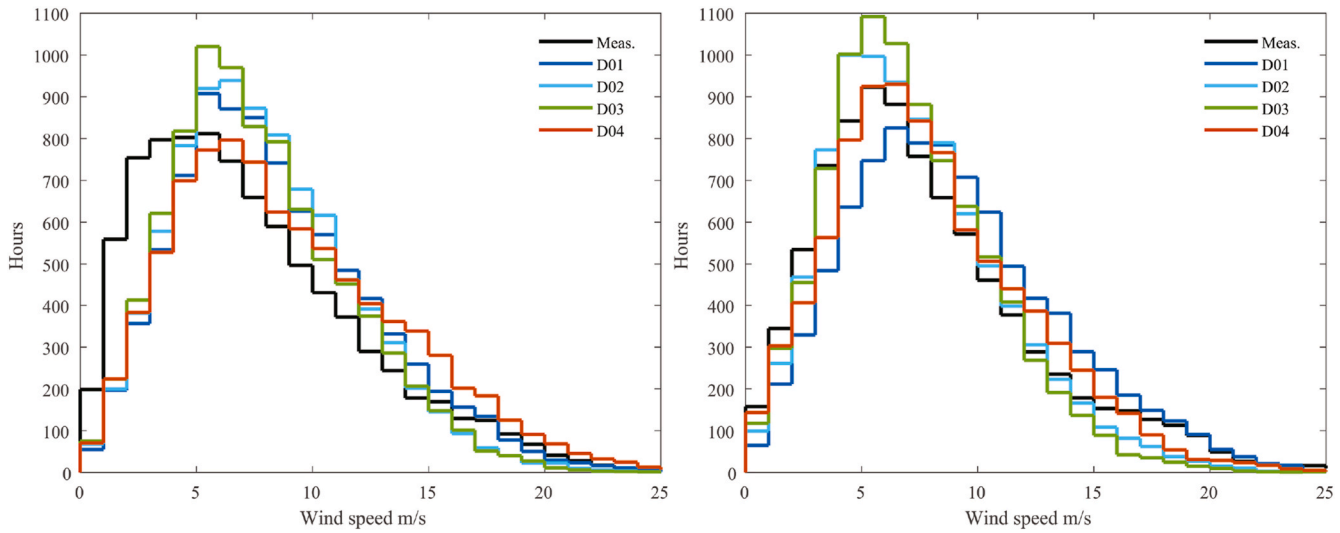

Fig. 5. Histograms for the measured wind speed (black line) and the simulations from domain D01 (dark blue), D02 (light blue), D03 (green) and D04 (red), for location B (left) and C (right).

locations, there are little improvements in the SD when forcing the simulations with ERA5 rather than ERA-I. The SD is very similar for the two model configurations, but appears to be sensitive to changes in the model resolution.

The wind roses for location B and C, presented in Fig. 4, provide a visual comparison of the cumulative distribution of the wind speed in combination with the wind direction. Only the simulations retrieved from the innermost domain with the highest resolution are considered in this figure. Location A is not presented here as the wind roses show very similar features as the nearby location B.

The measured wind data for location B, show a main wind direction from SE with a frequency above 10%, and a second main wind direction, with lower frequency, from the southwest (SW). The wind roses for both simulations, forced by either ERA-I or ERA5, show very similar features and are both able to reproduce the distribution of the measured wind well. Both wind roses show a high occurrence of wind from SE and high occurrence of wind from SW. Both models show a low occurrence of wind with a northerly component, in agreement with the measurements.

The wind rose for the measured data in location C shows a high occurrence of wind from two wind directions, the first from SE and the second from the south. The measured wind from SE has a high frequency of wind speed above 15 ms^{-1}, as well as wind speeds exceeding 20 ms^{-1}. The simulations are able to capture the main wind direction from SE, although slightly clockwise rotated compared to the measurements. The ERA5-forced simulations are in better agreement with the measurements than the simulations forced by ERA-I, as it shows a higher frequency of wind from this direction, including higher wind speeds above 15 ms^{-1}. The higher frequency of wind speed above 15 ms^{-1} from SE in the ERA5 forced simulations can be explained by a more detailed representation of the temperature over land in the ERA5 dataset in comparison to ERA-I (not shown), that may give rise to more pressure driven channelling of the air out the Lyngen fjord.

3.2. Evaluation of increasing model resolution

The ability of the model to reproduce the temporal variations of the measurements, as the grid resolution increases over the four domains, is also presented in the Taylor diagrams and as graphs in Fig. 3. For all locations, the correlation coefficient R tends to increases slightly when the distance between the grid spacing is reduced over the four domains. However, the correlation between the simulations and the measurements appears to be more sensitive to the choice of initialisation data, than it is to the resolution, particularly for location C. The CRMSE, the RMSE and the MAE improve at all locations when the grid spacing is reduced from D01 via D02 to D03. In particular, at locations A and B, the reduction of the unsystematic error, the CRMSE, is small, and similar to the correlation, appears to be more sensitive to the choice of initial and boundary conditions than the resolution. The wind speed simulations for location C, appear to have a higher sensitivity to the resolution than the other two locations, as the reduction in CRMSE over the first three domains is more prominent. In contrast, and for all locations, when the resolution is increased further, from 3 km in D03 to 1 km in D04, the MAE, the RMSE and the CRMSE increases considerably. In particular, the CRMSE is higher in D04 than in D01 for location A and B. Other studies also report similar results related to the model resolution, with clear improvements in the statistical evaluation metrics, as the resolution increases up to a certain threshold (Mass et al., 2002; Siuta et al., 2017). When the resolution is increased beyond this threshold, the improvement is less evident, and depends on the metrics used for evaluation as well as the location evaluated. A similar behaviour can be seen for the bias for location A and B in Fig. 3. The positive bias decreases as the grid spacing is decreased from 27 km via 9 km–3 km. When the grid spacing is further decreased to 1 km, the bias increases to its highest value for the two locations. At location C, the D01 simulations show the largest overestimation, while the lowest bias is found in D04. The SD of the simulations, also presented in Fig. 3, for all locations, are closest to the SD of the measurements in domain D01 and D04. For locations A and B, the wind simulations in D04 are able to reproduce the spread in wind speeds better than the other simulations, with an SD slightly larger than the SD of the measurements. In location C the SD closest to the SD of the measurements is found in domain D01.

In order to further assess how the change in grid spacing affects the quality of the model simulations in this study, the mean features are evaluated using frequency histograms and wind roses. In consideration of content limits, only the results from the ERA5 data will be considered in this section as similar results were found for the ERA-I data. Histograms for the measured and simulated wind speeds are presented in Fig. 5 for location B (left) and C (right). The x-axis shows the different wind speed bins, while the y-axis shows the frequency in number of hours. By comparing the histograms for location B, it is evident that all domains underestimate the frequency of the wind speeds below 5 ms^{-1}, and hence are all the histograms for the simulations shifted to the right and towards higher wind speeds. This is also reflected by the positive bias for all domains at this location. The first three domains, D01, D02, and, especially D03, overestimate the intermediate wind speeds between 5 ms^{-1} and 10 ms^{-1}. D01 is able to reproduce the occurrence of

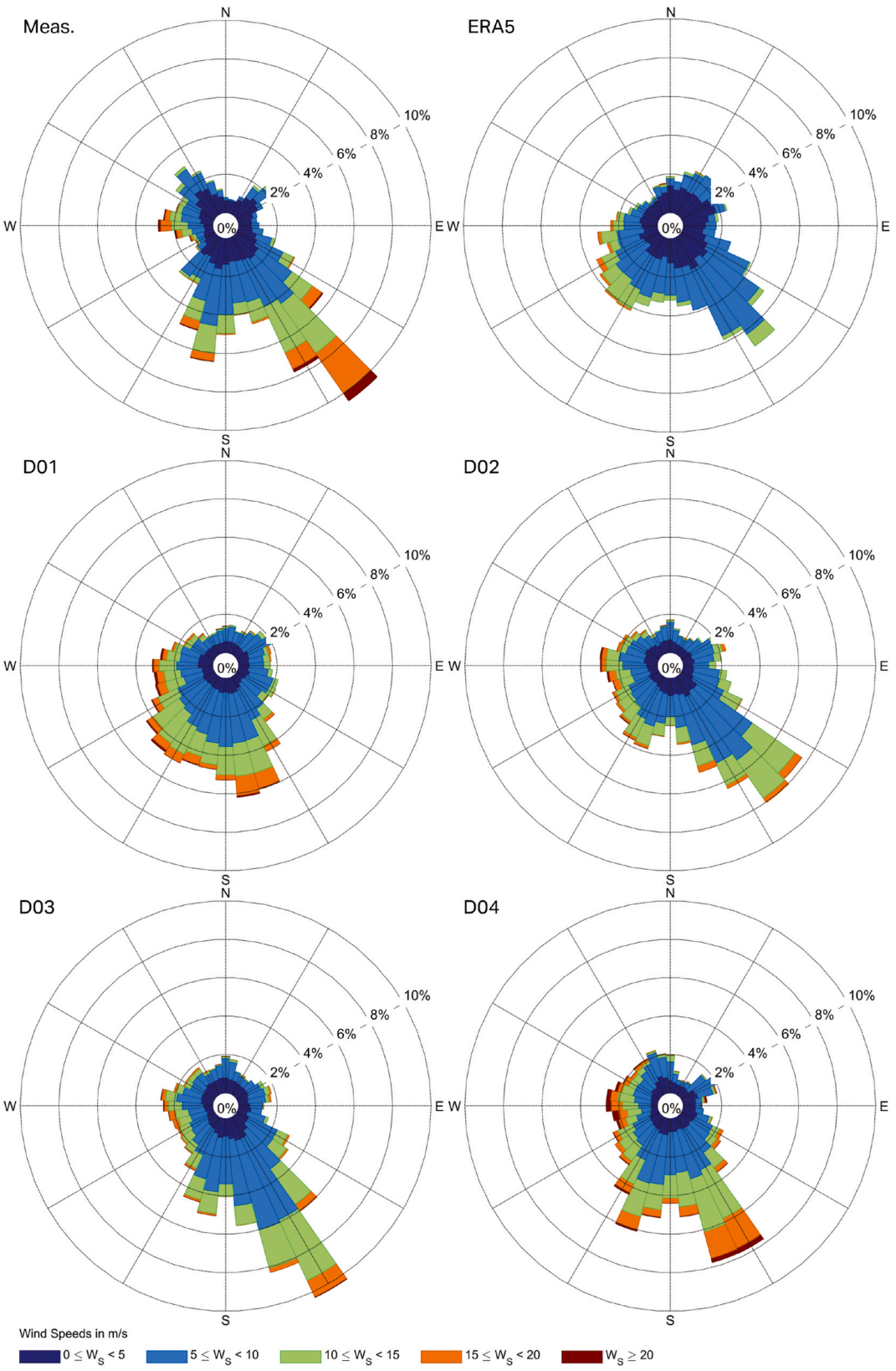

Fig. 6. Wind roses for the measurements (Meas), the original ERA5 data, and the simulations retrieved from domain D01, D02, D03 and D04 at location B.

the higher wind speeds above 15 ms^{-1} well, while D02 and D03 show an underestimation of the same wind speeds. This coincides well with the SD for the different domains, where the low SD found for D02 and D03 indicates a low spread of the wind speeds, and the higher SD for D01 indicates that the simulations are able to capture the spread of the wind speed better. The shape of the histogram for D04 shows a great resemblance with the histogram of the measurements, although with a shift to the right. While the wind speed histograms for all the simulations at

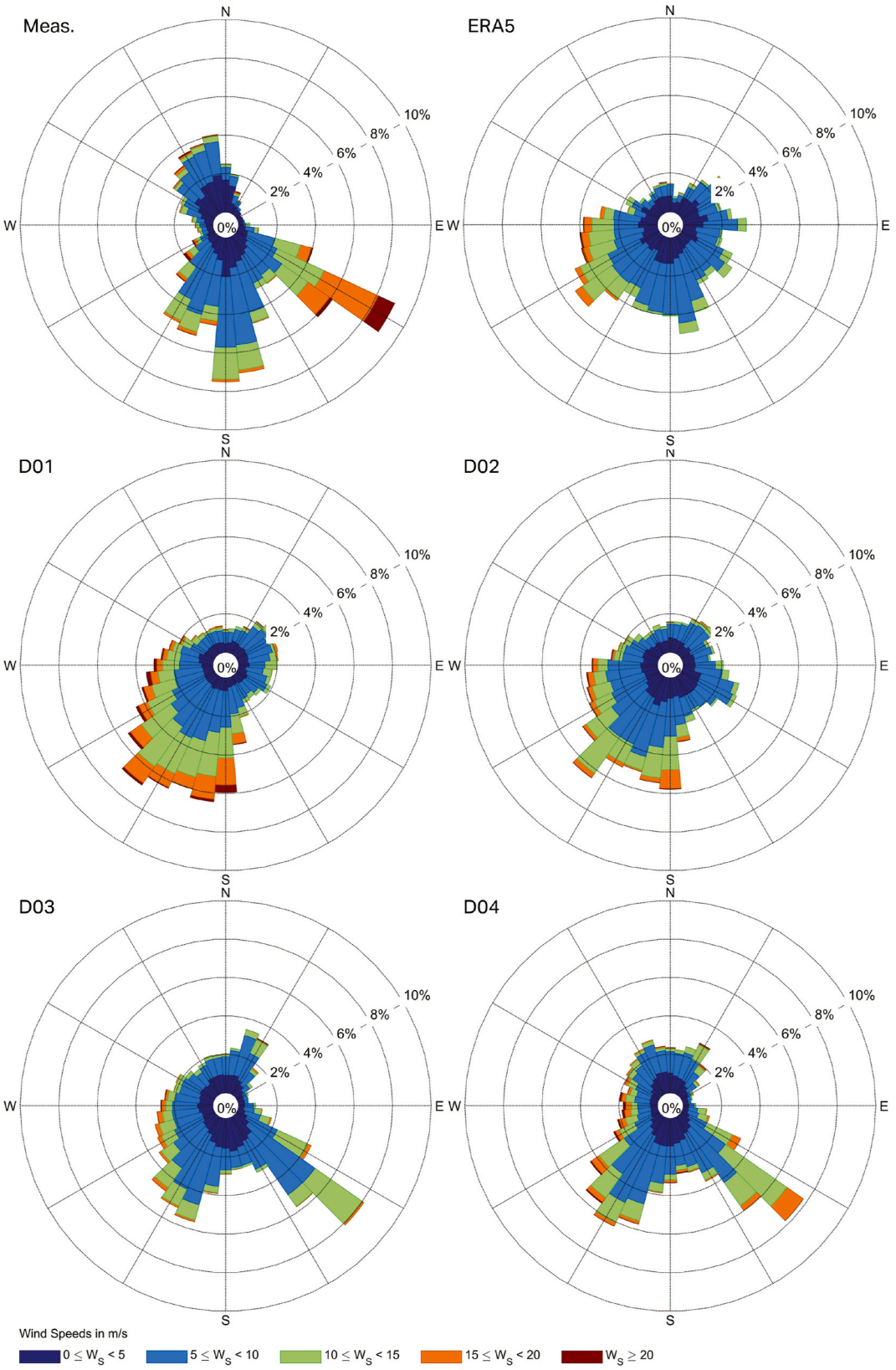

Fig. 7. Wind roses for the measurements (Meas), the original ERA5 data, and the simulations retrieved from domain D01, D02, D03 and D04 at location C.

location B are skewed to the right compared to the measurements, only the winds from the D01 simulations are skewed to the right for location C. The histograms for the other three domains, that also have a considerable lower bias than D01, show a more similar shape to the histogram of the measurements. Similar to the situation at location B, D02 and D03 overestimate the intermediate wind speeds at location C, and underestimate the higher wind speeds. The histogram of the wind speeds retrieved from D04 shows a better agreement between the

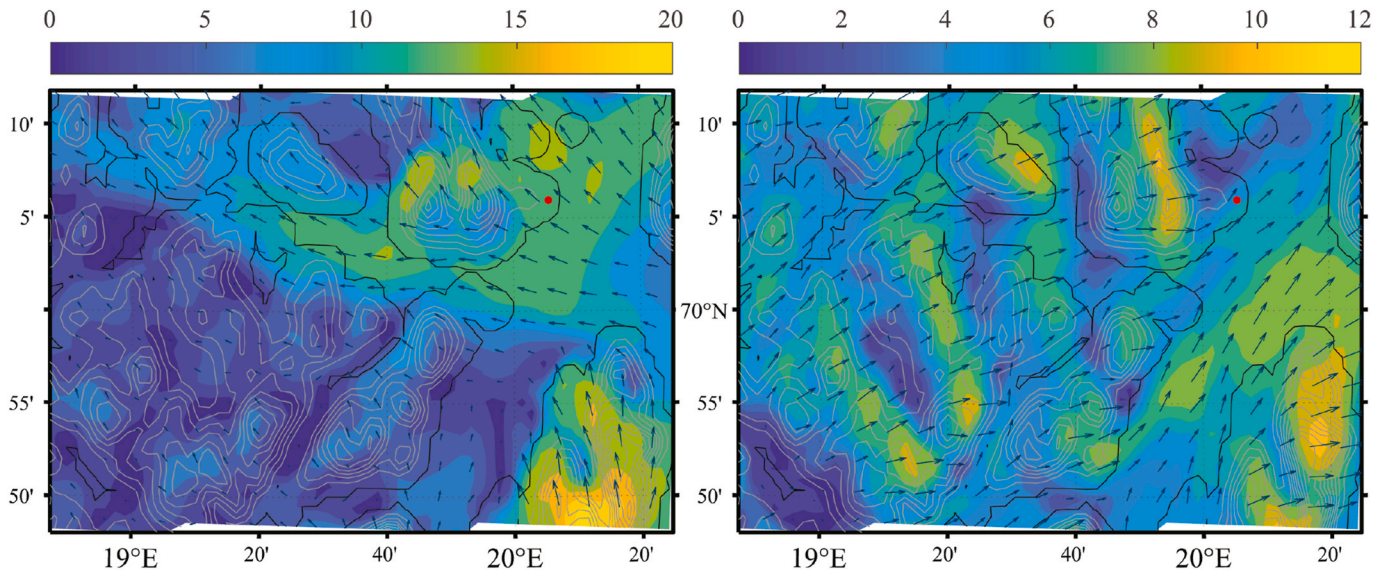

Fig. 8. Colour maps showing the D04 wind speed and direction at 80 magl. on 20 December 2014 (left) and 13 May 2015 (right). Arrows indicate the wind direction. The contour lines show the elevation with 100 m between each line. The red dot in the maps depict location C.

simulated wind speed and the measurements, than the wind speeds from the simulations with a coarser resolution.

To also evaluate how the simulated wind speed in combination with wind direction are affected by the increased resolution, wind roses for location B and C are presented in Figs. 6 and 7, respectively. The figures include wind roses for the measurements and for the wind data retrieved from all four domains. In addition, the figures also include wind roses for the original 100 magl. ERA5 wind data. The wind components are retrieved from the exact locations by bilinear interpolation.

First the wind roses for location B in Fig. 6 will be considered. The wind rose presenting the original ERA5 data shows a high occurrence of wind from SE. This is in agreement with the measured main wind direction from SE, although with a lower frequency. The ERA5 model is not able to reproduce any of the higher wind speeds above 15 ms^{-1} present in the measurements. This illustrates the limitations of global reanalyses, like ERA-I and ERA5, to reproduce local wind, especially in complex terrain, and why direct use of the reanalysis data should be avoided in the assessment of local wind speeds (Olauson, 2018; Ramon et al., 2019). The D01 domain appears to be an improvement compared to ERA5 for the frequency of wind speeds above 10 ms^{-1}, but not for the main wind direction, as the wind direction is spread almost evenly over a large sector stretching from west to SE. The large difference between the ERA5 model and the selected configuration of the WRF model D01, with almost similar horizontal resolution, can probably be related to differences in e.g. domain sizes, terrain representation, physiography and parametrization of physical processes. A more detailed investigation of these differences, although relevant for wind simulations, is not further elaborated in this paper, since the main focus is on the effect of the increased horizontal resolution in the WRF model.

The finer resolution simulations, D02, D03, and D04, are able to reproduce the main wind direction from SE better than D01 compared to the measurements. The frequency of wind speeds between 15 ms^{-1} and 20 ms^{-1} from SE is low in D02 and increases slightly in D03. D04 has a higher frequency of the same wind speeds, in better agreement with the measurements, and is also able to reproduce some of the wind speeds above 20 ms^{-1}. The observed frequency of wind directions from the SW is more apparent in D03 and D04 compared to the coarse-resolution models. However, the frequency of winds from SW are better reproduced in D04 compared to D03. The wind roses for the measurements, in both location A (not shown) and location B, show a low occurrence of wind from a sector stretching from about 225° to 255° (W-SW). In particular, there is a very low occurrence of wind speeds above 10 ms^{-1}. One explanation for the low occurrence of wind from W-SW, can be orographic blocking by the steep mountains on the island Senja. The low occurrence of wind from W-SW are not captured well in any of the simulations, although slightly better in D03 and D04 in comparison with the simulations with coarser resolutions. The poor representation of wind in this sector can be related to the terrain representation by the model. In reality, the mountains on Senja reach up to a 1000 masl. whereas in the four models they are represented with lower elevations. For instance, in D04, altitudes only up to 700 masl. represent the same mountains. This indicates that a better terrain representation, perhaps also even higher horizontal model resolution, is needed to resolve the terrain effect upstream of location A and B.

In Fig. 7, the wind data for location C is presented. The ERA5 wind data, and the two WRF simulations, D01 and D02, have winds mainly coming from one large sector stretching from the west to the south. D01 has, compared to the ERA5 data and the other WRF simulations, a higher frequency of all wind speeds above 10 ms^{-1}. The two higher resolution domains, D03 and D04, are able to reproduce the main wind direction from SE, although slightly clockwise rotated compared to the measurements. D04 has a higher frequency of wind speeds between 15 ms^{-1} and 20 ms^{-1} from SE than D03, and are in better agreement with the measurements. None of the simulations are able to capture the highest wind speeds above 20 ms^{-1} present in the measurements from SE.

In the measurements, there is a high occurrence of wind directly from the south. This is not represented in either D03 or D04. Instead, in both the finer-resolution simulations, there is a higher frequency of wind from SW in comparison to the measurements. The behaviour of an air flow approaching a mountain barrier depends on the atmospheric stability, the wind speed and the characteristics of the mountain, such as the height (Whiteman, 2000). The differences in wind patterns can therefore be related to the representation of the terrain in the models. For instance, the lack of wind from the south in the simulations can be related to unresolved topography in the Lyngen Alps (See Fig. 1) upstream of location C that causes too much orographic blocking of the wind from the south. Another explanation can be related to the model terrain representations of the mountains west of location C. The mountains reach up to 1000 masl. and under varying atmospheric conditions, winds from the west can, for instance, be forced around the mountains or lifted over the mountains. In the D04 terrain, the same mountains west of location C, has a maximum elevation of 750 masl.

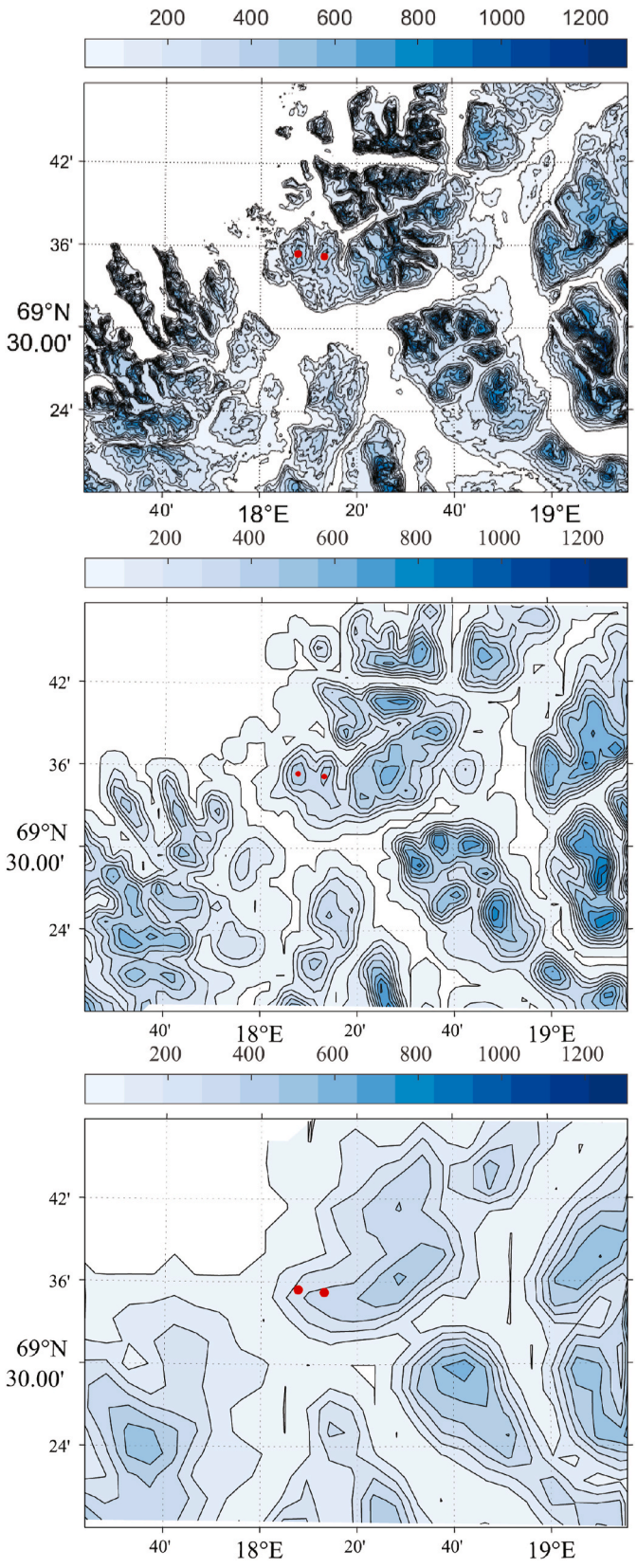

Fig. 9. Top: Terrain map with a 50-m resolution. Middle: Model representation of the terrain elevation in domain D04 with 1 km resolution. Bottom: Model representation of the terrain elevation in domain D03 with 3 km resolution. Ocean in white and the different blue colours represent elevations. Location A (left) and B (right) are indicated by red dots.

This considerably lower model terrain, can give rise to a slightly different wind pattern at location C, where e.g. less blocking of the air leads to stream across instead of around the mountains. Two shorter time periods have been selected to illustrate a possible explanation to the lack of winds from the south in the D04 simulations in location C.

In the first period selected, from 19–20 December 2014, the measured wind direction is from the south and the wind speed varies between 0 ms^{-1} and 8 ms^{-1}. The D04 simulation, in the same time period, has wind from SE and the wind speed is overestimated and varies between 7 ms^{-1} and 15 ms^{-1}. In the second selected time period, on 13 May 2015 00:00 to 12.00 local time, the measured wind direction is also from the south, however, the D04 simulations show wind from SW. The measured wind speed varies 0 ms^{-1} and 7 ms^{-1}, while the simulated wind speeds varies between 3 ms^{-1} and 7 ms^{-1}. In Fig. 8 the D04 wind simulations from 80 magl. at and around location C is presented for 20 December 2014 04:00 local time (left) and 13 May 03:00 local time (right). On the 20 December the wind field has a strong easterly component in the fjord east of locations C and a green field of wind speeds of approximately 12 ms^{-1} in the same location. Closer to location C and the nearby mountains, there is a field of lower wind speeds and the wind vectors turns towards SE. A more accurate terrain representation may lead to more blocking of the air flow approaching from the west, hence lower wind speed in location C, and force more of the air flow around the mountain in a northward direction. On 13 May, as can be seen in Fig. 8, the air flow approaches the mountains nearby location C from the west. The wind vectors are not affected by the mountain barrier and there is a field of higher wind speed on the mountain tops, indicating that the air flow passes over the mountains. A more accurate representation of the terrain, with higher mountains may result in more of the air flow to be forced around instead of over the mountains west of location C, and be deflected northwards on the lee side of the mountains.

In addition, as can be seen in the wind roses in Fig. 7, the numerical simulations have a higher occurrence of wind directly from the west at location C, compared to the measurements. West of the mast in location C, the mountains with elevations up to 1000 masl. might cause an orographic blockage of wind from the west. Domain D04 is able to capture some of this orographic blockage, with a low frequency of wind from this direction, although with intermediate and high wind speeds present. However, at certain atmospheric conditions and wind speeds, strong downslope winds might occur. It must therefore also be taken into consideration that the measurements, in particular wind speeds from the west, might be disturbed by the nearby wind farm.

3.2.1. *Case study*

Based on the evaluation of the different horizontal model resolutions, so far in this study, the positive impact of an increased resolution from D03 to D04 is unclear. While the wind speed histograms and the wind roses show an improved representation of the mean features in D04 compared to D03, for all locations, A, B and C, the CRMSE, the RMSE, the MAE, and the bias indicate the opposite. A higher resolution and a more realistic representation of the terrain are e.g. expected to improve the simulations of terrain induced wind effects. However, the method of comparing point measurements with interpolated model information might be limited by timing and spatial errors of meteorological features, like mountain waves and gap winds, that become more prominent with increased horizontal resolution (Mass et al., 2002). In particular, when using traditional verification metrics to compare measurements and simulations in points, spatial errors may be penalized both for the absence of the observed wind pattern, but also for the presence of a wind pattern that is not observed at the location (Zingerle and Nurmi, 2008). This “double penalty” might not be seen when the resolution is lower as the wind features tend to be more smoothed (Zingerle and Nurmi, 2008). In order to further analyse the effect of increased horizontal resolution from 3 km to 1 km, a case study has been carried out for location A and B. Fig. 9 shows a close up map of the real terrain (top) and the model topography (D04 in the middle and D03 at

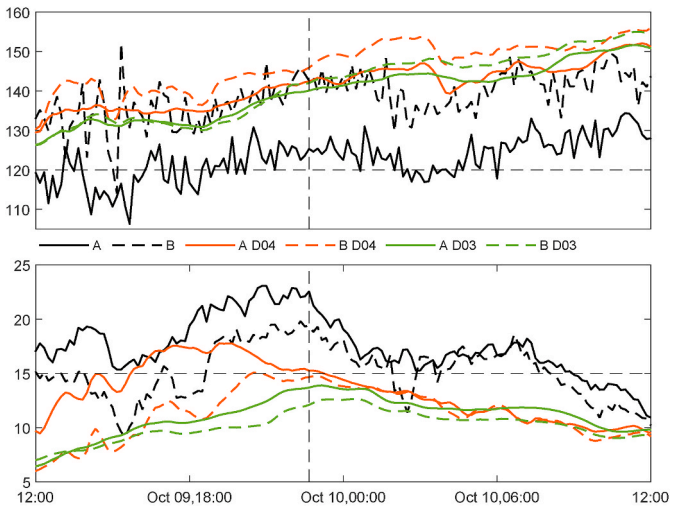

Fig. 10. Wind direction (top) and wind speed (bottom) for location A and B on 9 October 2014. The vertical dotted line indicate the time of the wind map presented in Fig. 11.

the bottom). The maps include location A and B indicated by red dots. From Fig. 9 it is clear that the topography is much better resolved in D04 compared to D03. When the terrain of D04 is compared to the real terrain, it is clear that even at 1 km horizontal resolution, considerable parts of the orography are not resolved. In particular, there is a height difference between the real topography and the topography of D04 of 82 m at location A and 75 m at location B (Table 1).

Fig. 10 shows the wind speed and the wind direction of location A and B, over a 24-h period, starting at noon on the 9 October 2014. The measured wind is coming from SE, the main wind direction, between 120° and 150°. The measured wind speeds at both locations are high, with long periods over 15 ms^{-1} at both locations, and also over 20 ms^{-1} at location A. The simulations are able to reproduce the wind direction in both D03 and D04 well, while the wind speed, especially from about 18:00 local time on 9 October 2014, is considerably underestimated. Moreover, after about 20:00 only small differences can be found in the wind speed when the resolution is increased from D03 to D04.

In particular, during the 5 h time period from about 20:00 on the 9 October 2014 to 01:00 the following day, there are observed stronger winds at location A than at location B. Neither the high wind speed, or the difference in wind speeds between the two locations, are represented by D03 or D04. In order to study this in detail, Fig. 11 shows a close up map of the wind speed and direction 9 October at 22:40, for D03 (left) and D04 (right). D03 has small variations of the wind speeds, with one large green coloured area representing wind speeds between 10 and 14 ms^{-1} covering both the fjord SW of location A and B, and the locations of the measurements. In D04, we can identify larger variations in the wind speeds. Location A and B are both included in a light green area with wind speeds in the interval 14–16 ms^{-1}, and just downwind of location A we find a yellow area with wind speeds up to 20 ms^{-1}. Although, this strong wind field does not include location A, from the wind map in Fig. 11 it is evident that D04 are able to reproduce strong winds in close vicinity of location A, while the strong winds are not seen in D03. The strong down slope wind seen downwind of location A, can e.g. be a result of mountain wave activity. Mountain waves are reported to have the possibility to severely impact wind power production, as they can cause large spatial and temporal fluctuations in wind speeds (Draxl et al., 2021; Xia et al., 2021). The case study presented here exemplifies how high resolution wind simulations can provide more detailed information that are useful, both for wind resource wind mapping and wind prediction in complex terrain.

4. Conclusion

In this study, wind simulations provided by the WRF model, have been evaluated in an area characterized by a coastal and complex terrain located in Northern Norway. In specific, the aim of this study has been to evaluate the performance of the simulations when either forced by ERA-I or ERA5, both provided by the ECMWF, as well as to evaluate the impact different grid spacings has on the wind simulations. The wind simulations have been compared to hub-height wind measurements at three locations. It was found that the ERA5 forced simulations provided lower MAE, RMSE and CRMSE and higher correlation, in comparison to the ERA-I forced simulations. The WRF simulations were run with four one-way nested domains, D01, D02, D03 and D04, with horizontal resolution of 27 km, 9 km, 3 km and 1 km, respectively. The results showed that when the resolution was increased from 27 km, via 9 km to 3 km, the MAE, the RMSE, the CRMSE and the bias decreased, while the correlation increased. When the grid spacing was further decreased, from 3 km

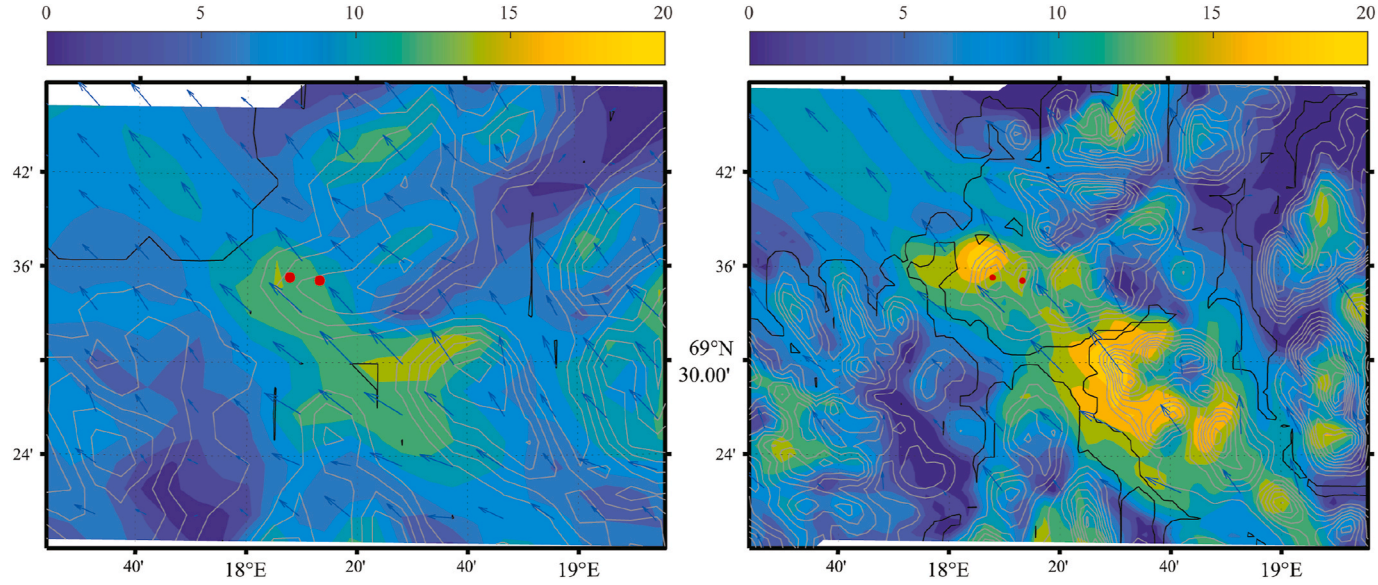

Fig. 11. Colour maps showing wind speed and direction on 9 October 2014 at 22:40 for domain D03 (left) and D04 (right). Arrows indicate the wind direction. The contour lines show the elevation with 100 m between each line. The two red dots in the maps depict location A (left) and B (right).

to 1 km, the MAE, the RMSE and the CRMSE at the three locations were impaired. It is suggested that the lack of improvement from the 3 km to the 1 km simulations, could be due to timing and spatial errors that occur when comparing measurements and simulations from a fixed geographical point. Further research should evaluate how different PBL schemes affect the results regarding increased model resolution. Nevertheless, the wind speed histograms and the wind roses show that the D04 simulations, with 1 km resolution, provide an improved reproduction of the mean features of the wind and the variations in the wind speed, in comparison with the simulations with lower resolution. In addition, a case study show that although the high wind speed events are not reproduced at the exact same locations as the measurements, the highest-resolution simulations show fields of higher wind speeds in nearby locations that coincides with the measured wind event, whereas D03 is not able to reproduce these terrain effects. This result exemplifies that although the highest resolution simulations scores low on the traditional statistical measures such as MAE, RMSE, CRMSE and bias, the higher resolution simulations appears to reproduce local terrain effects better than the simulations run with a coarser resolution. A limitation of this study is that only wind measurements at one height, 80 magl. is considered. A further study should include measurements of the vertical wind profile and an evaluation of the ability of the WRF model to reproduce the wind shear in complex terrain, in particular wind shear that might be harmful for wind turbines.

Declaration of competing interest

The authors declare that they have no known competing financial interests or personal relationships that could have appeared to influence the work reported in this paper.

Acknowledgements

This work is supported by Troms county and industry development fund under the project title, “Renewable energy in the Arctic – academy and business in a joint effort” RDA12/46. The authors would like to thank Nordlys Vind and Troms Kraft for the meteorological data used in this work.

Appendix

Table A.1
Summary of the statistical measures presented in Fig. 3. In the bias column, the bold value is the mean measured wind speed and in the SD column, the bold value is the SD of the measurements.

		Bias		SD		R		MAE		RMSE		CRMSE	
		ERA-I	ERA5	ERA-I	ERA5	ERA-I	ERA5	ERA-I	ERA5	ERA-I	ERA5	ERA-I	ERA5
A		**7.86**		**4.98**									
A	D01	0.75	0.55	4.2	4.15	0.53	0.58	3.51	3.25	4.56	4.27	4.5	4.24
A	D02	0.31	0.09	3.85	3.77	0.55	0.59	3.33	3.15	4.32	4.12	4.31	4.12
A	D03	0.3	0.08	4.03	3.96	0.56	0.61	3.29	3.06	4.3	4.04	4.29	4.04
A	D04	1.83	1.6	5.2	5.1	0.57	0.63	3.83	3.39	5.07	4.63	4.73	4.34
B		**7.39**		**4.64**									
B	D01	1.21	1.07	4.27	4.25	0.53	0.6	3.46	3.17	4.48	4.16	4.31	4.02
B	D02	0.73	0.58	3.87	3.82	0.54	0.58	3.24	3.02	4.2	3.97	4.14	3.93
B	D03	0.49	0.38	3.84	3.82	0.56	0.62	3.11	2.87	4.05	3.77	4.02	3.75
B	D04	1.69	1.61	4.84	4.85	0.57	0.63	3.61	3.28	4.74	4.41	4.42	4.1
C		**7.82**		**4.69**									
C	D01	1.16	1.13	4.48	4.54	0.43	0.5	3.93	3.67	5.03	4.75	4.9	4.61
C	D02	−0.36	−0.43	3.75	3.8	0.45	0.51	3.39	3.21	4.52	4.28	4.51	4.26
C	D03	−0.79	−0.69	3.47	3.53	0.49	0.59	3.28	2.96	4.34	3.92	4.27	3.86
C	D04	0.01	0.17	4.17	4.23	0.49	0.58	3.43	3.13	4.5	4.11	4.5	4.1

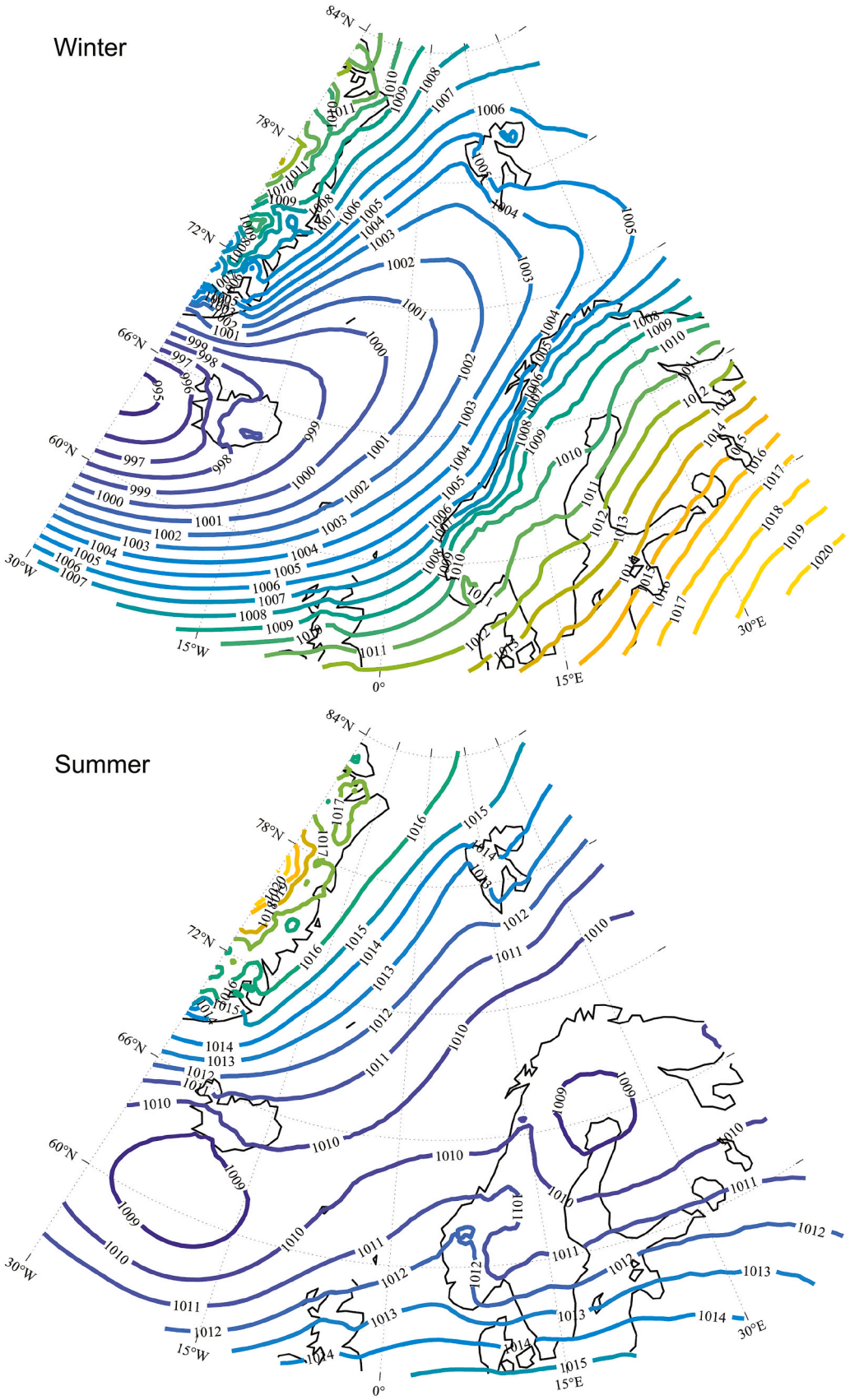

Fig. A.1. Top: MSLP during the winter months from September 2014 to March 2015 obtained from the ERA5 reanalysis. Bottom: Same as above, but for summer months April 2015 to August 2015.

References

Awan, N.K., Truhetz, H., Gobiet, A., 2011. Parameterization-induced error characteristics of MM5 and WRF operated in climate mode over the alpine region: an ensemble-based analysis. J. Clim. 24 (12), 3107–3123. https://doi.org/10.1175/2011JCLI3674.1.

Belmonte Rivas, M., Stoffelen, A., 2019. Characterizing ERA-Interim and ERA5 surface wind biases using ASCAT. Ocean Sci. 15 (3), 831–852. https://doi.org/10.5194/os-15-831-2019.

Berge, E., Nyhammer, F., Tallhaug, L., Jacobsen, Ø., 2006. An evaluation of the WAsP model at a coastal mountainous site in Norway. Wind Energy 9 (1–2), 131–140. https://doi.org/10.1002/we.191.

Bowen, A., Mortensen, N., 1996. Exploring the limits of WAsP the wind atlas analysis and application program, 1996. In: Zervos, A., Ehmann, H., Helm, P. (Eds.), European Union Wind Energy Conference. Proceedings. H.S. Stephens and Associates, pp. 584–587, 1996 European Wind Energy Conference and Exhibition, EWEC '96 ; Conference date: 20-05-1996 Through 24-05-1996.

Byrkjedal, Ø., Åkervik, E., 2009. Vindkart for norge (in Norwegian). Tech. rep. 10. The Norwegian Water Resources and Energy Directorate (NVE).

Carvalho, D., Rocha, A., Gómez-Gesteira, M., 2012a. Ocean surface wind simulation forced by different reanalyses: comparison with observed data along the Iberian Peninsula coast. Ocean Model. 56, 31–42. https://doi.org/10.1016/j.ocemod.2012.08.002.

Carvalho, D., Rocha, A., Gómez-Gesteira, M., Santos, C., 2012b. A sensitivity study of the WRF model in wind simulation for an area of high wind energy. Environ. Model. Software 33, 23–34. https://doi.org/10.1016/j.envsoft.2012.01.019.

Carvalho, D., Rocha, A., Gómez-Gesteira, M., Silva Santos, C., 2014. WRF wind simulation and wind energy production estimates forced by different reanalyses: comparison with observed data for Portugal. Appl. Energy 117, 116–126. https://doi.org/10.1016/j.apenergy.2013.12.001.

Chen, F., Janjić, Z., Mitchell, K., 1997. Impact of atmospheric surface-layer parameterizations in the new land-surface scheme of the NCEP mesoscale eta model. Boundary-Layer Meteorol. 85, 391–421. https://doi.org/10.1023/A:1000531001463.

Dee, D.P., Uppala, S.M, Simmons, A.J., Berrisford, P., Poli, P., Kobayashi, S., Andrae, U., Balmaseda, M.A., Balsamo, G., Bauer, P., Bechtold, P., Beljaars, A.C.M., van de Berg, L., Bidlot, J., Bormann, N., Delsol, C., Dragani, R., Fuentes, M., Geer, A.J., Haimberger, L., Healy, S.B., Hersbach, H., Hólm, E.V., Isaksen, L., Kållberg, P., Köhler, M., Matricardi, M., McNally, A.P., Monge-Sanz, B.M., Morcrette, J.-J., Park, B.-K., Peubey, C., de Rosnay, P., Tavolato, C., Thépaut, J.-N., Vitart, F., 2011. The ERA-Interim reanalysis: configuration and performance of the data assimilation system. Q. J. R. Meteorol. Soc. 137 (656), 553–597. https://doi.org/10.1002/qj.828.A.

Draxl, C., Worsnop, R.P., Xia, G., Pichugina, Y., Chand, D., Lundquist, J.K., Sharp, J., Wedam, G., Wilczak, J.M., Berg, L.K., 2021. Mountain waves can impact wind power generation. Wind Energy. Sci. 6 (1), 45–60. https://doi.org/10.5194/wes-6-45-2021.

Fernández-González, S., Martín, M.L., García-Ortega, E., Merino, A., Lorenzana, J., Sánchez, J.L., et al., 2018. Sensitivity analysis of the WRF model: wind-resource assessment for complex terrain. J. Appli. Meteorol. Climatol. 57 (3), 733–753. https://doi.org/10.1175/JAMC-D-17-0121.1.

Graham, R.M., Hudson, S.R., Maturilli, M., 2019. Improved performance of ERA5 in arctic gateway relative to four global atmospheric reanalyses. Geophys. Res. Lett. 46 (11), 6138–6147. https://doi.org/10.1029/2019GL082781.

Hersbach, H., Bell, B., Berrisford, P., Hirahara, S., Horányi, A., Muñoz-Sabater, J., Nicolas, J., Peubey, C., Radu, R., Schepers, D., Simmons, A., Soci, C., Abdalla, S., Abellan, X., Balsamo, G., Bechtold, P., Biavati, G., Bidlot, J., Bonavita, M., De Chiara, G., Dahlgren, P., Dee, D., Diamantakis, M., Dragani, R., Flemming, J., Forbes, R., Fuentes, M., Geer, A., Haimberger, L., Healy, S., Hogan, R., Hólm, E., Janisková, M., Keeley, S., Laloyaux, P., Lopez, P., Lupu, C., Radnoti, G., de Rosnay, P., Rozum, I., Vamborg, F., Villaume, S., Thépaut, J.-N., 2020. The ERA5 global reanalysis. Q. J. R. Meteorol. Soc. 146 (730), 1999–2049. https://doi.org/10.1002/qj.3803.

Iacono, M.J., Delamere, J.S., Mlawer, E.J., Shephard, M.W., Clough, S.A., Collins, W.D., 2008. Radiative forcing by long-lived greenhouse gases: calculations with the AER radiative transfer models. J. Geophys. Res.: Atmosphere 113 (D13). https://doi.org/10.1029/2008JD009944.

Inoue, J., Yamazaki, A., Ono, J., Dethloff, K., Maturilli, M., Neuber, R., Edwards, P., Yamaguchi, H., 2015. Additional Arctic observations improve weather and sea-ice forecasts for the Northern Sea Route. Sci. Rep. 5 (16868), 1–8. https://doi.org/10.1038/srep16868.

Jacobson, M.Z., 2005. Introduction. Fundamentals of Atmospheric Modeling, second ed. Cambridge University Press, pp. 1–11. Ch. 1.

Janjić, Z.I., 1994. The step-mountain eta coordinate model: further developments of the convection, viscous sublayer, and turbulence closure schemes. Mon. Weather Rev. 122 (5), 927–945. https://doi.org/10.1175/1520-0493(1994)122<0927:TSMECM>2.0.CO;2.

Krieger, J.R., Zhang, J., Atkinson, D.E., Zhang, X., Shulski, M.D., 2009. Sensitivity of WRF model forecasts to different physical parametrizations in the Beaufort Sea region. In: The Eighth Conference on Coastal Atmospheric and Oceanic Prediction and Processes.

Mass, C.F., Ovens, D., Westrick, K., Colle, B.A., 2002. Does increasing horizontal resolution produce more skillful forecasts?: the results of two years of real-time numerical weather prediction over the pacific northwest. Bull. Am. Meteorol. Soc. 83 (3), 407–430. https://doi.org/10.1175/1520-0477(2002)083<0407:DIHRPM>2.3.CO;2.

Menéndez, M., Tomás, A., Camus, P., García-Díez, M., Fita, L., Fernández, J., Méndez, F. J., Losada, I.J., 2011. A methodology to evaluate regional-scale offshore wind energy resources. In: OCEANS 2011. IEEE, Spain, pp. 1–8.

Mughal, M.O., Lynch, M., Yu, F., McGann, B., Jeanneret, F., Sutton, J., 2017. Wind modelling, validation and sensitivity study using Weather Research and Forecasting model in complex terrain. Environ. Model. Software 90, 107–125. https://doi.org/10.1016/j.envsoft.2017.01.009.

National Research Council, 1992. Coastal Meteorology A Review of the State of the Science. National Academies Press. https://doi.org/10.17226/1991.

Olauson, J., 2018. ERA5: the new champion of wind power modelling? Renew. Energy 126, 322–331. https://doi.org/10.1016/j.renene.2018.03.056.

Powers, J.G., Klemp, J.B., Skamarockck, W.C., Davis, C.A., Dudhia, J., Gill, D.O., Coen, J. L., Gochis, D.J., Ahmadov, R., Peckckham, S.E., Grell, G.A., Michalakes, J., Trahan, S., Benjamin, S.G., Alexander, C.R., Dimego, G.J., Wang, W., Schwartz, C.S., Romine, G.S., Liu, Z., Snyder, C., Chen, F., Barlage, M.J., Yu, W., Duda, M.G., 2017. The weather research and forecasting model: overview, system efforts, and future directions. Bull. Am. Meteorol. Soc. 98 (8), 1717–1737. https://doi.org/10.1175/BAMS-D-15-00308.1.

Ramon, J., Lledó, L., Torralba, V., Soret, A., Doblas-Reyes, F.J., 2019. What global reanalysis best represents near-surface winds? Q. J. R. Meteorol. Soc. 145 (724), 3236–3251. https://doi.org/10.1002/qj.3616.

Romine, G.S., Schwartz, C.S., Snyder, C., Anderson, J.L., Weisman, M.L., 2013. Model bias in a continuously cycled assimilation system and its influence on convection-permitting forecasts. Mon. Weather Rev. 141 (4), 1263–1284. https://doi.org/10.1175/MWR-D-12-00112.1.

Samuelsen, E.M., 2007. Et dynamisk studium av stormen Narve - et kaldluftsutbrudd i Finnmark - ved hjelp av observasjoner og numeriske simuleringer (In Norwegian).

Siuta, D., West, G., Stull, R., 2017. WRF hub-height wind forecast sensitivity to PBL scheme, grid length, and initial condition choice in complex terrain. Weather Forecast. 32 (2), 493–509. https://doi.org/10.1175/WAF-D-16-0120.1.

Skamarock, W.C., Klemp, J.B., Dudhia, J., Gill, D.O., Barker, D.M., Duda, M.G., Huang, X.-Y., Wang, W., Powers, J.G., 2008. A Description of the Advanced Research WRF Version 3. NCAR TECHNICAL NOTE, NCAR/TN–475+STR.

Svendsen, H., 1995. Physical oceanography of coupled fjord-coast systems in northern Norway with special focus on frontal dynamics and tides. In: Skjoldal, H.R., Hopkins, C., Erikstad, K.R., Leinaas, H.P. (Eds.), Ecology of Fjords and Coastal Waters. Elsevier, Amterdam, pp. 149–164.

Taylor, K.E., 2001. Summarizing multiple aspects of model performance in a single diagram. J. Geophys. Res.: Atmosphere 106 (D7), 7183–7192. https://doi.org/10.1029/2000JD900719.

Thompson, G., Field, P.R., Rasmussen, R.M., Hall, W.D., 2008. Explicit forecasts of winter precipitation using an improved bulk microphysics scheme. Part II: implementation of a new snow parameterization. Mon. Weather Rev. 136 (12), 5095–5115. https://doi.org/10.1175/2008MWR2387.1.

Tiedtke, M., 1989. A comprehensive mass flux scheme for cumulus parameterization in large-scale models. Mon. Weather Rev. 117 (8), 1779–1800. https://doi.org/10.1175/1520-0493(1989)117<1779:ACMFSF>2.0.CO;2.

Valkonen, T., Stoll, P., Batrak, Y., Køltzow, M., Schneider, T.M., Stigter, E.E., Aashamar, O.B., Støylen, E., Jonassen, M.O., 2020. Evaluation of a sub-kilometre NWP system in an Arctic fjord-valley system in winter. Tellus Dyn. Meteorol. Oceanogr. 72 (1), 1–21. https://doi.org/10.1080/16000870.2020.1838181.

Wesslén, C., Tjernström, M., Bromwich, D.H., de Boer, G., Ekman, A.M.L, Bai, L.S., Wang, S.H., 2014. The Arctic summer atmosphere: an evaluation of reanalyses using ASCOS data. Atmos. Chem. Phys. 14 (5), 2605–2624. https://doi.org/10.5194/acp-14-2605-2014.

Whiteman, C.D., 2000. Mountain Meteorology: Fundamentals and Applications. Oxford University Press, Incorporated.

Wilks, D., 2011. Statistical Methods in the Atmospheric Sciences, International Geophysics. Elsevier Science.

Xia, G., Draxl, C., Raghavendra, A., Lundquist, J.K., 2021. Validating simulated mountain wave impacts on hub-height wind speed using sodar observations. Renew. Energy 163, 2220–2230. https://doi.org/10.1016/j.renene.2020.10.127.

Zhang, C., Wang, Y., Hamilton, K., 2011. Improved representation of boundary layer clouds over the southeast pacific in ARW-WRF using a modified Tiedtke cumulus parameterization scheme. Mon. Weather Rev. 139 (11), 3489–3513. https://doi.org/10.1175/MWR-D-10-05091.1.

Zingerle, C., Nurmi, P., 2008. Monitoring and verifying cloud forecasts originating from operational numerical models. Meteorol. Appl. 15 (3), 325–330. https://doi.org/10.1002/met.73.